JOURNAL OF AIRCRAFT
Vol. 46, No. 2, March–April 2009

Numerical and Experimental Analysis of a Generic Fan-in-Wing Configuration

Nicolas Thouault,* Christian Breitsamter,† and Nikolaus A. Adams‡
Technical University of Munich, 85747 Garching, Germany

DOI: 10.2514/1.39750

The present investigation focuses on assessing the predictive capabilities of state-of-the-art computational fluid dynamics for a generic fan-in-wing configuration by comparison with experimental data. The objective is to reproduce a short take off and landing or a transition-flight situation without ground effect. A rotating fan is placed in the wing plane, inside of the wing's rear part and close to the root section. The obtained experimental data include force measurements, surface pressure measurements, flowfield mapping using particle image velocimetry and wool-tufts visualization. A structured mesh of the entire configuration with minimum geometrical simplifications is used to perform unsteady Reynolds-averaged Navier–Stokes computations. The area surrounding the rotor blades is set up as sliding mesh to simulate the rotation. Because of the abrupt deflection of the flow by the fan, an unsteady recirculation area is generated above the rotor blades resulting in a highly distorted inflow. The blocking of the freestream by the jet exiting the fan's nozzle creates a back pressure affecting the internal aerodynamics. The jet rolls up in a counter-rotating vortex pair with considerable impact on the wing's aerodynamic performance. Time-averaged unsteady results over one fan revolution show a good agreement with the experimental data. The major turbulence phenomena are well predicted by the simulation.

Nomenclature

b	=	wingspan, m
c	=	root chord, m
C_D	=	drag coefficient
C_L	=	lift coefficient
C_m	=	pitching moment coefficient with respect to the quarter chord
C_p	=	pressure coefficient
C_T	=	thrust coefficient, $T/(0.5\rho U_\infty^2 S)$
D_f	=	fan diameter, m
M	=	Mach number
M_∞	=	freestream Mach number
N	=	fan rotational speed, rpm
Re_c	=	Reynolds number based on the root chord
S	=	planform area, m^2
T	=	fan thrust, N
t	=	wing maximum thickness, m
U_x	=	streamwise velocity component, m/s
U_∞	=	freestream velocity, m/s
x, y, z	=	streamwise, spanwise, and vertical coordinate directions, m
y_+	=	dimensionless wall distance
α	=	angle of attack, deg
θ	=	angular position around the fan, deg
μ	=	tip-speed ratio, $U_\infty/(\pi N D_f/60)$
μ_t	=	eddy viscosity, Pa/s
ρ	=	density, kg/m^3
ω	=	vorticity, 1/s
$\bar{\omega}$	=	dimensionless vorticity, $\bar{\omega} = \omega/(2U_\infty/D_f)$

Received 14 July 2008; revision received 31 October 2008; accepted for publication 8 November 2008.

*Research Engineer, Institute of Aerodynamics. Member AIAA.
†Chief Scientist, Institute of Aerodynamics. Associate Fellow AIAA.
‡Professor, Institute of Aerodynamics. Member AIAA.

I. Introduction

THE fan-in-wing concept was originally proposed to allow for short/vertical takeoff and landing (S/VTOL) missions. It was implemented in the jet powered experimental aircraft Ryan GE XV-5 in the 1960s. Many experimental investigations on fan-in-wing configurations can be found in NASA technical notes. Most of them are related to the development of the Ryan GE XV-5. A good overview of the investigations and summary of the main results are provided in [1–3]. These studies point out the complexity of the flow due to the fan being installed in the wing. For instance, the inflow distortion [4] and the back pressure at the fan nozzle [5] are critical parameters for such configurations. The interaction of the jet with the freestream is also a major issue because it bears a strong similarity to the jet-in-crossflow problem albeit in classical setups crossflow mass fluxes are commonly much smaller. The jet-in-crossflow has received considerable attention during the last years, particularly concerning its application in S/VTOL aircraft. Several phenomena can be observed [6], such as a jet deflected by the freestream, jet blockage, and entrainment. A review of previous investigations of aerodynamic effects induced by a jet on a fan powered S/VTOL aircraft in hover and transition flight is given in [7]. Four major vortical structures have been established in comprehensive jet-in-crossflow analysis: 1) horseshoe vortices formed upstream of the jet exit and wrapping around the jet column [8–10], 2) wake vortices [8], 3) jet shear layer vortices formed also upstream of the jet [10], and 4) a pair of counter-rotating vortices located downstream of the jet exit [11]. The counter-rotating vortex pair is initiated near the jet nozzle [12,13] and is the dominating structure in the downstream flowfield [14]. Unsteady sliding mesh simulations of an embedded crossflow fan into a thick wing have recently been performed [15] and compared with experimental results [16]. This two-dimensional analysis differs from the flow topology of the fan-in-wing configuration investigated here. The present study focuses on a three-dimensional configuration with a fan rotating in the plane of a wing (Fig. 1). A fan composed of a rotor and a stator is located in the rear part of the wing. The fan ingests a part of the incoming flow boundary layer. After compression, the air is ejected through the nozzle, creating a jet in crossflow. A wide range of experimental results has been gathered in a previous study [17], including force and surface pressure measurements, flowfield mapping using particle image velocimetry (PIV), and wool-tufts visualization. The objective of the present investigation is a detailed flowfield analysis based on numerical results obtained by unsteady Reynolds-averaged

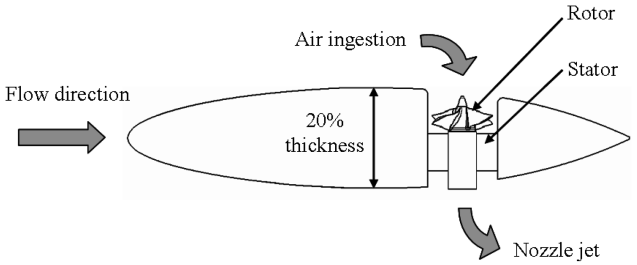

Fig. 1 Schematic view of the experimental setup.

Navier–Stokes (URANS) computations and a comparison with experimental data. In addition, a discussion concerning the fan efficiency is given.

II. Experimental Technique

In this section, the wind tunnel model and experiments are described.

A. Wind Tunnel Model

The model airfoil is of NACA 16-020 type. It provides enough space to insert two model fans inside the wing. The wing-half model has an aspect ratio of 2.3, a semispan area of 0.683 m^2, a taper ratio of 0.71, and 0 deg sweep of the 50% root chord line. The model is designed to investigate several generic fan-in-wing configurations: 1) the closed wing without the fan as reference, 2) one single fan installed either at the rear (Fig. 2) or in the front part of the wing, and 3) two fans placed symmetrically with respect to the half chord. The geometry modeled in the numerical simulation is the one presented in Fig. 2 for a single fan at the wing rear part. The rear fan axis is located at $\frac{2}{3}c$ and at $0.12b$ from the root chord. The fan has a diameter of $0.13c$. On the wing's upper side the lip radius to diameter was set as 8% (Fig. 3b). The model is installed on a peniche to raise the wing out of the wind tunnel wall boundary layer. The model fan is composed of two stages, a four-bladed rotor and four-bladed stator. The engine is located inside the stator and, therefore, gives a realistic configuration with no external device around the wing. The cables to provide power and to measure the engine temperature are fixed behind one stator blade trailing edge (Fig. 3a) to minimize their influence.

B. Wind Tunnel Data

All the results presented in this study concern the configuration in which a single fan is set at the wing's rear part (Fig. 2). A variety of experimental techniques were used to provide a reliable database for simulation validation. The experimental work has been performed in the Göttingen-type wind tunnel A at the Technical University of Munich. The test section dimensions are 1.8 m in height, 2.4 m in width, and 4.8 m in length. Maximum usable velocity is 65 m/s with a turbulence level of the freestream less than 0.4%. Four different types of tests have been conducted in the wind tunnel campaign: force measurements, surface static pressure measurements, flowfield mapping using stereo PIV near the trailing edge and wool-tufts flow visualization. For the force measurements, angle-of-attack polars were carried out between $\alpha = -10$ deg and $\alpha = 20$ deg, away from the stall region. PIV measurements were only carried out at a specific operating condition detailed in Sec. IV. Three different freestream velocities U_∞ have been investigated: 30 m/s, 40 m/s, and 50 m/s corresponding to a Reynolds number based on the root chord of $\mathrm{Re}_c = 1.5 \times 10^6$, $\mathrm{Re}_c = 2 \times 10^6$, and $\mathrm{Re}_c = 2.5 \times 10^6$, respectively. Three different fan rotation speeds were investigated: $N = 21,000$, 23,700, and 26,500 rpm. The wind tunnel balance precision is 0.025% with respect to the maximum loads (+1500 N for the drag, $+/-$ 3000 N for the lift, and $+/-$ 500 N · m for the pitching moment). Thus, the uncertainties in drag, lift, and pitching moment coefficients are +0.0011, $+/-$ 0.0022, and $+/-$ 0.0005, respectively.

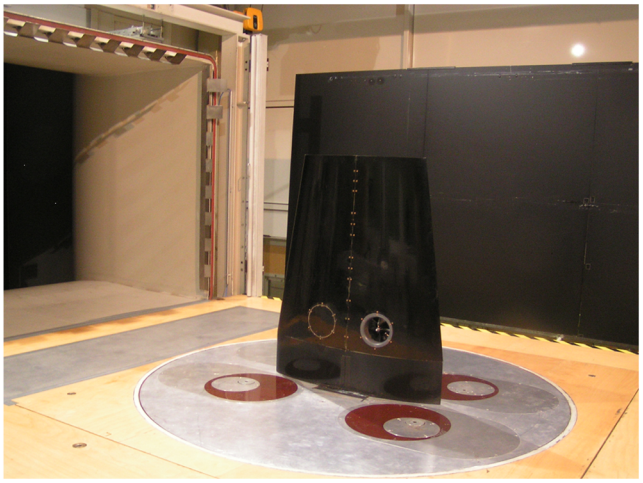

Fig. 2 Model setup in wind tunnel test section.

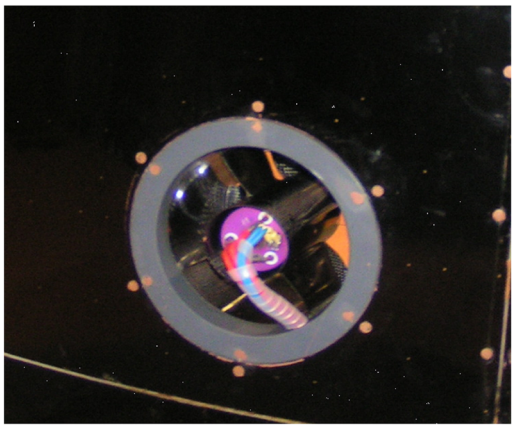

a)

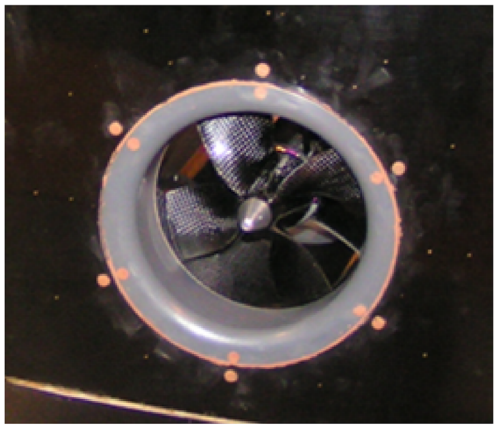

b)

Fig. 3 Model details showing a) the fan's exit, and b) inlet section.

III. Numerical Simulations

In this section, the numerical simulations are described.

A. Preprocessing

Here, the computational parameters are described and an analysis of the flow is given.

1. *Mesh Topology*

A multiblock structured mesh is generated around the geometry. The rotor blade geometry itself is highly twisted and requires

particular attention when creating mesh blocks. ANSYS ICEM CFD is used for this purpose. A block structured mesh has been selected to obtain more accurate results especially in the near-wall region. Special attention has been given to the nearest mesh node in the viscous sublayer for a good prediction of the separated regions on the wing and on the fan's blades. The mesh is constructed to benefit from a low Reynolds number near-wall formulation. A value of $y_+ < 1$ is achieved for the attached flow on the wing and fan's blade surfaces. On the inlet lip and the rotor blade tips, the value of y_+ remains below four. Overall, 939 blocks were created. This number of blocks is necessary to avoid negative volumes and to obtain a relatively good mesh quality in terms of orthogonality, minimum angle, and aspect ratio. The geometry requires an unconventional blocking strategy. An O-grid topology is set around each fan blade and around the wing. The overall computational topology is a C-H topology, commonly used for external aerodynamic numerical simulation. Ten chords were used in each direction from the wing to create the computational domain [18,19]. Special care has been taken to create a continuous blocking for the entire geometry to avoid different surface meshes between blocks. Surface meshes on the wing and on the rotor are presented in Fig. 4. Geometrical simplifications cannot be avoided considering the complexity of the geometry. A representation of the wires providing power to the engine is neglected. Located behind one stator blade trailing edge (Fig. 3a), they are assumed to have only a small influence on the overall results. The fan's geometry is simplified to create a suitable blocking around the geometry. The gaps between the rotor and stator and the holes are removed. The rotor blade fillets are also neglected. Thus, the blade geometry in the hub vicinity is extrapolated. Despite these changes, the rest of the geometry is precisely modeled, including the clearance gap between the rotor blade tip and the shroud housing to capture secondary flows. The clearance gap is 0.8% of the fan's diameter.

2. *Simulation Setup*

ANSYS CFX flow simulation software is used to perform CFD simulations of this fan-in-wing configuration. A second-order discretization of the convective terms is used throughout all calculations. The k-ω shear stress transport model of Menter [20] is used for all computations. To simulate the fan's rotation during steady calculations, a reference frame transformation between the area surrounding the blades and the rest of the computational domain is done by frozen-rotor interfaces [21]. In this case, the results depend on the initial position of the blade and do not describe accurately the rotor/stator interaction. For the unsteady calculation, the area surrounding the blades is designated as sliding mesh. Sliding interfaces separate the rotating domain from the stationary domain (Fig. 5). The interaction between the rotor and stator is, thus, taken into account and, therefore, provides a more realistic model. The root-mean-square residuals are less than 10^{-5} for continuity and less than 10^{-4} for all other residuals (heat transfer, momentum, and turbulence quantities). The total energy model is used to account for compressibility effects, especially significant at the rotor blade tip and on the inlet radius. The maximum Mach number in this area approaches $M \approx 0.7$. The initial data for the unsteady run are obtained by performing a steady calculation. Unsteady simulations require a proper time-step limit, resulting in a compromise between computational time and numerical accuracy. A full revolution requires 286 time steps for the baseline mesh. All the unsteady results presented in this paper represent time-averaged data over one fan rotor revolution. A number of 24 CPUs on a 512-node Altix cluster is used, with a computational time of about 1000 CPU h for the steady simulation and 3500 CPU h for the unsteady case, corresponding approximately to five complete rotor revolutions for the baseline mesh. After five revolutions, the variation of the time-averaged loads over a revolution is negligible. A history of the wing's loads is presented in Fig. 6.

For the wing without a fan, a symmetry condition can be set at the wing's root chord plane. With a fan, a symmetry condition at this position is not used. Instead, the peniche is included in the computational domain for all the simulations. An isothermal model is used instead of the total energy model ($M < 0.15$). A free slip wall boundary condition is applied to model the wind tunnel floor. The effect of the wind tunnel floor is assumed to have a negligible

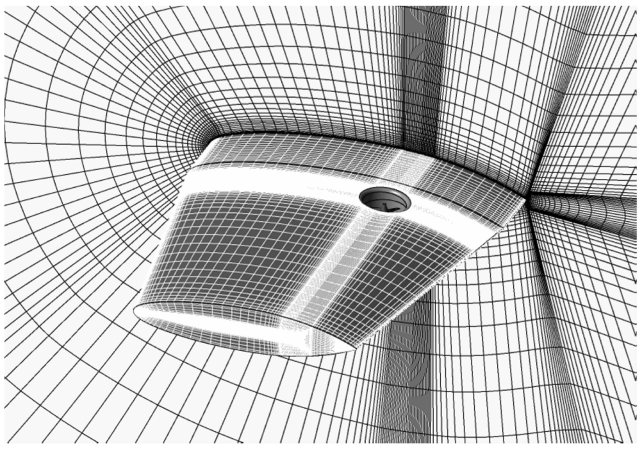

a)

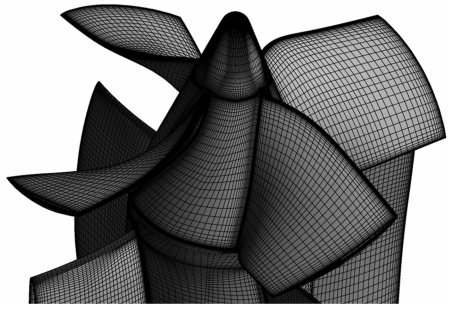

b)

Fig. 4 Surface mesh on a) the wing, and b) the rotor blades and hub.

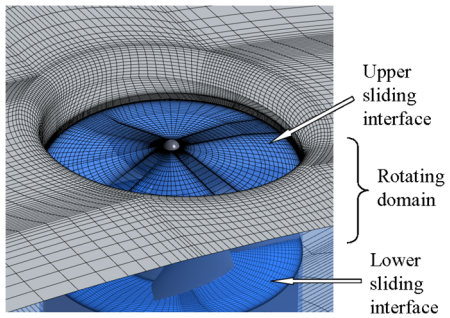

Fig. 5 Position of sliding interfaces, inlet lip, and wing upper-side mesh.

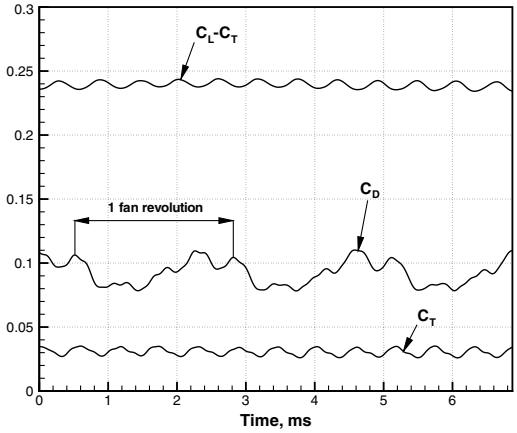

Fig. 6 Time history of aerodynamic coefficients.

influence on the wing. No boundary layer mesh is thus generated on the wind tunnel floor, consequently reducing the computational cost.

3. Grid-Resolution Study

For the steady solution, all forces acting on the body eventually oscillate around a mean value. The grid-resolution study is presented considering these mean values. Three different mesh resolutions are tested: a coarse grid of 2.6×10^6 nodes, a medium grid of 4×10^6 nodes, and a fine grid of 9×10^6 nodes. Relevant dimensions and spacings of the grids are given in the Table 1. The grid refinement is performed in the wing's normal direction. In addition, the number of grid points around the airfoil is increased, especially on its rear part, to enhance the mesh density in the region of the jet mixing with the crossflow. Finally, a significant refinement is made in the fan region to evaluate the grid dependence of the thrust and the pressure rise. This last refinement is made in each direction. The solver performs an automatic near-wall treatment and switches from a wall function to a low Reynolds number wall formulation as the mesh is refined. As previously stated, the mesh is established to benefit from the low Reynolds wall formulation. The value of y_+ remains, therefore, similar for all grids. The forces predicted with the finer mesh are closer to the experimental results. According to Table 2, the comparison of the steady results shows only a small difference between the medium and fine grid. Therefore, all the calculations are performed with the 4×10^6 nodes medium grid. The steady calculation using a frozen-rotor approach cannot predict accurately the fan's behavior due to the strong unsteadiness on the blade loading generated by a large inflow distortion. However, it provides a very good initial solution for the external aerodynamics, particularly the loads on the wing, which are the main focus here. Mass flow rate and total pressure rise are comparable to the unsteady results. A frozen-rotor method as well as an actuator disk approach can significantly reduce the computational effort and provide a valuable tool to investigate different wing arrangements.

B. Unsteady Results

All the results presented in this section refer to a freestream velocity of $U_\infty = 40$ m/s ($\mathrm{Re}_c = 2 \times 10^6$) and a fan rotation speed of $N = 26,200$ rpm, which corresponds to a tip-speed ratio of $\mu = 0.243$. The angle of attack is $\alpha = 0$ deg to isolate the fan's contribution and the induced aerodynamic effects on the overall flow.

1. Flow Topology

Streamlines are presented for a plane cutting the fan's center (Fig. 7). The numerical results show that the main features encountered in a jet in crossflow, as listed in the introduction, are predicted by the simulation. The adverse pressure gradient formed at the fan's exit causes the wall boundary layer to separate and, therefore, create the horseshoe vortex (Fig. 7, spot a). The horseshoe vortex wraps around the jet column (cf. Fig. 17b). The incoming flow on the wing's upper side is strongly entrained by the jet. Thus, the flow remains attached at the trailing edge (Fig. 7, spot b), and the flow separates at about 93% of the chord for the closed wing without a fan at $\alpha = 0$ deg. The fan has the capability to maintain attached flow at the wing's trailing edge in a small region downstream of the inlet lip (cf. Fig. 17a). The existence of a saddle point on the leeward side of the jet is predicted by the simulation (Fig. 7, spot c). The streamlines from this saddle point indicate a small flow region close to the wing's surface following the streamwise direction. Further downstream another saddle point is predicted (Fig. 7, spot d). The recirculation area below the hub at the fan's exit is also predicted. On the wing's upper side, the streamline visualization indicates the presence of two stagnation areas, located at the hub nose and on the inlet lip downstream of the fan, respectively. The flow separates at the inlet lip upstream of the fan. A further analysis of the separation bubble (Fig. 7, spot e) occurring above the rotor blade is given in the next sections. Figure 8 shows isosurfaces of the time-averaged dimensionless vorticity magnitude as seen from the opposite streamwise direction. The vorticity is nondimensionalized using the fan's radius as characteristic length. The characteristic time considered is, therefore, $D_f/2U_\infty$. The roll up of the jet in a counter-rotating vortex pair (CVP) can clearly be observed in Fig. 8b, for a vorticity magnitude $\bar{\omega} = 0.9$. The CVP originates from the wing's lower side downstream of the nozzle (Fig. 8a). The strong entrainment due to the CVP is evident from Fig. 8c. This entrainment increases the kinetic energy on the wing's upper side downstream of the fan's inlet. Thus, the flow remains attached in this area as observed in Fig. 7. The flow phenomenology in the near field on the wing's lower side is described in Fig. 9. This sketch has been established using time-averaged results. As stated before, a horseshoe vortex wraps around the jet column. The horseshoe vortex is not convected to the trailing edge but disappears rapidly near each side of the fan's exit. Counter-rotating vortices emanate from each side of the fan's exit. The CVP is well established downstream of the wing and near the trailing edge. At about $x/c = 1$, the CVP is the only vortical structure observed, and it dominates the downstream flow. The flow near the wall is immediately entrained in the jet column, close behind the nozzle. Downstream of the saddle point located near the fan's exit (Fig. 7, spot c), the flow remains attached on the wing, and a small flow layer near the wall follows the streamwise direction to a certain extent before being entrained in the direction of the windward side of the jet. Backward velocities of significant magnitude are observed inside the counter-rotating vortex pair. Near the trailing edge and between the CVP, the flow separates and forms two vertically oriented vortical structures in the wake of

Table 1 Details of the grid employed for the fan-in-wing case

Parameters	Coarse grid	Medium grid	Fine grid
Normal layers in C-H mesh	35	51	85
Averaged y_+ over the wing	1.15	0.70	0.68
Wrap-around points	190	200	285
Leading-edge spacing/c	0.0052	0.0040	0.0031
Trailing-edge spacing/c	1.9×10^{-4}	1.4×10^{-4}	1.0×10^{-4}
Nodes in the fan's region, $\times 10^6$	1.2	1.6	3.9
Total number of nodes, $\times 10^6$	2.6	4	9

Table 2 Comparison of aerodynamic coefficients for different grid levels [$\alpha = 0$ deg, $U_\infty = 40$ m/s, and $N = 26,200$ rpm ($\mu = 0.243$)]

Parameters	Coarse grid	Medium grid	Fine grid	Experimental
C_L	0.258	0.266	0.268	0.298
C_D	0.093	0.094	0.095	0.101
C_m	−0.035	−0.037	−0.039	−0.055
C_T	0.036	0.037	0.037	-

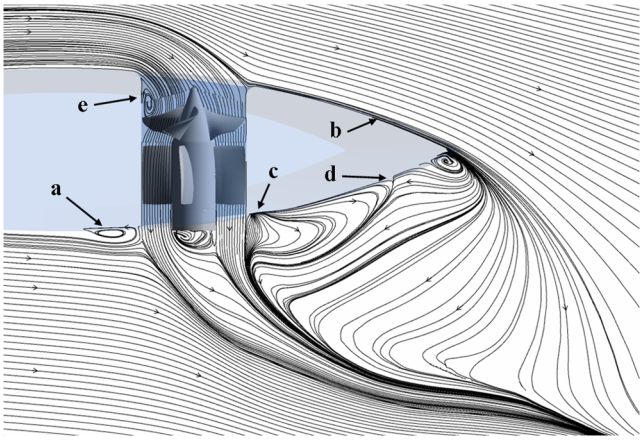

Fig. 7 Streamlines of a spanwise section located at 0.12*b* [$\alpha = 0$ deg, $U_\infty = 40$ m/s, and $N = 26,200$ rpm ($\mu = 0.243$)]; flow from left to right.

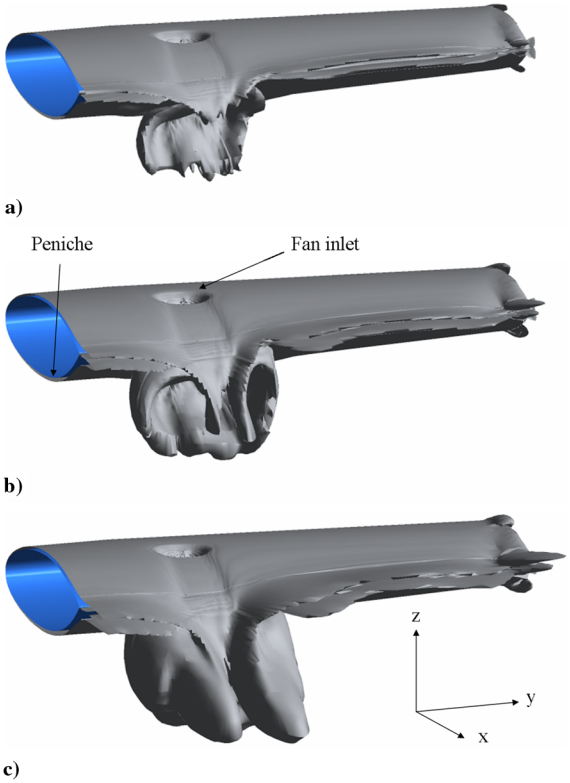

Fig. 8 Isosurfaces of time-averaged vorticity magnitude a) $\bar{\omega} = 1.5$, b) $\bar{\omega} = 0.9$, and c) $\bar{\omega} = 0.5$ [$\alpha = 0$ deg, $U_\infty = 40$ m/s, and $N = 26,200$ rpm ($\mu = 0.243$)].

the jet. This phenomenon occurs due do the strong entrainment of the CVP.

2. *Inflow Distortion*

The abrupt deflection of the flow by the fan is causing a nonuniform inflow velocity profile. The area upstream of the fan's inlet features high velocities, whereas downstream of the hub nose a low-velocity area is present. Separation occurs on the inlet lip, therefore, generating a recirculation area above the rotor blades with a low Mach number in its core (Fig. 10a). The asymmetric velocity distribution (with respect to the fan's center line) reveals an advancing and retreating flow condition on the rotor blades. Note that the fan's rotational sense is counterclockwise as seen from above. The time-averaged pressure coefficient distribution on the wing and inlet lip shows also retreating and advancing flow conditions and reveals that the pressure distribution above the rotor blade is highly distorted (Fig. 10b). This distortion is confirmed by the circumferential pressure distributions (Fig. 10c). The distortion is weak and almost symmetric to $\theta = 0$ deg for circumferential line a, whereas it is strong for circumferential lines b and c. As shown by the streamlines on Fig. 7, the presence of stagnation areas on the hub nose and downstream of the fan on the inlet lip, respectively, is confirmed by the time-averaged pressure coefficient distribution. The pressure gradient is significant on the inlet lip due to the abrupt flow deflection. The rotor blade experiences tip stall when the blade begins to retreat (Fig. 11). This phenomenon does not appear in the time-averaged results. Note that Fig. 11a represents the streamlines based on the time-averaged velocity. Figures 11b–11d show the streamlines on the blades based on the instantaneous calculations for several time steps (thus several rotor positions). Based on this result, the stall region is indicated in Fig. 11d. This region clearly depends on the advancing and retreating flow condition because of its asymmetric behavior. The tip stall experienced by the rotor blade is linked to the recirculation area provoked by the flow separation on the inlet lip. The stall area as well as the recirculation bubble show an unsteady behavior due to the fan rotation. The pressure load on the rotor blades is also highly distorted and unsteady. This pressure distribution modifies the fan characteristic point and considerably reduces its efficiency compared with an ideal inflow.

3. *Crossflow at the Fan's Exit*

The jet interaction with the crossflow at the fan's exit affects the fan's efficiency. The jet generated by the fan blocks the freestream and, therefore, increases the pressure in a region upstream of the jet nozzle (Fig. 12a). A back pressure at the fan exit is present. The C_p contours of the time-averaged pressure coefficient in the stator surroundings confirm this last conclusion. The back pressure at the exit is indicated by the pressure distribution of Fig. 12c. The section in Fig. 12b is located right beneath the rotating domain. At this location, the nonuniform pressure distribution is caused mainly by

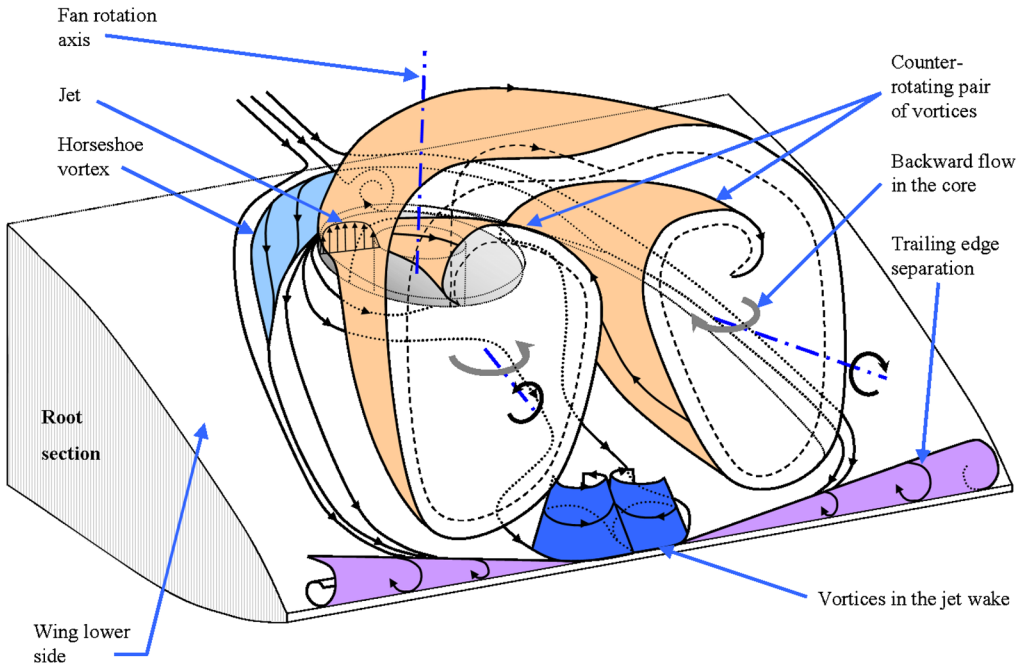

Fig. 9 Flow topology sketch for the wing lower side.

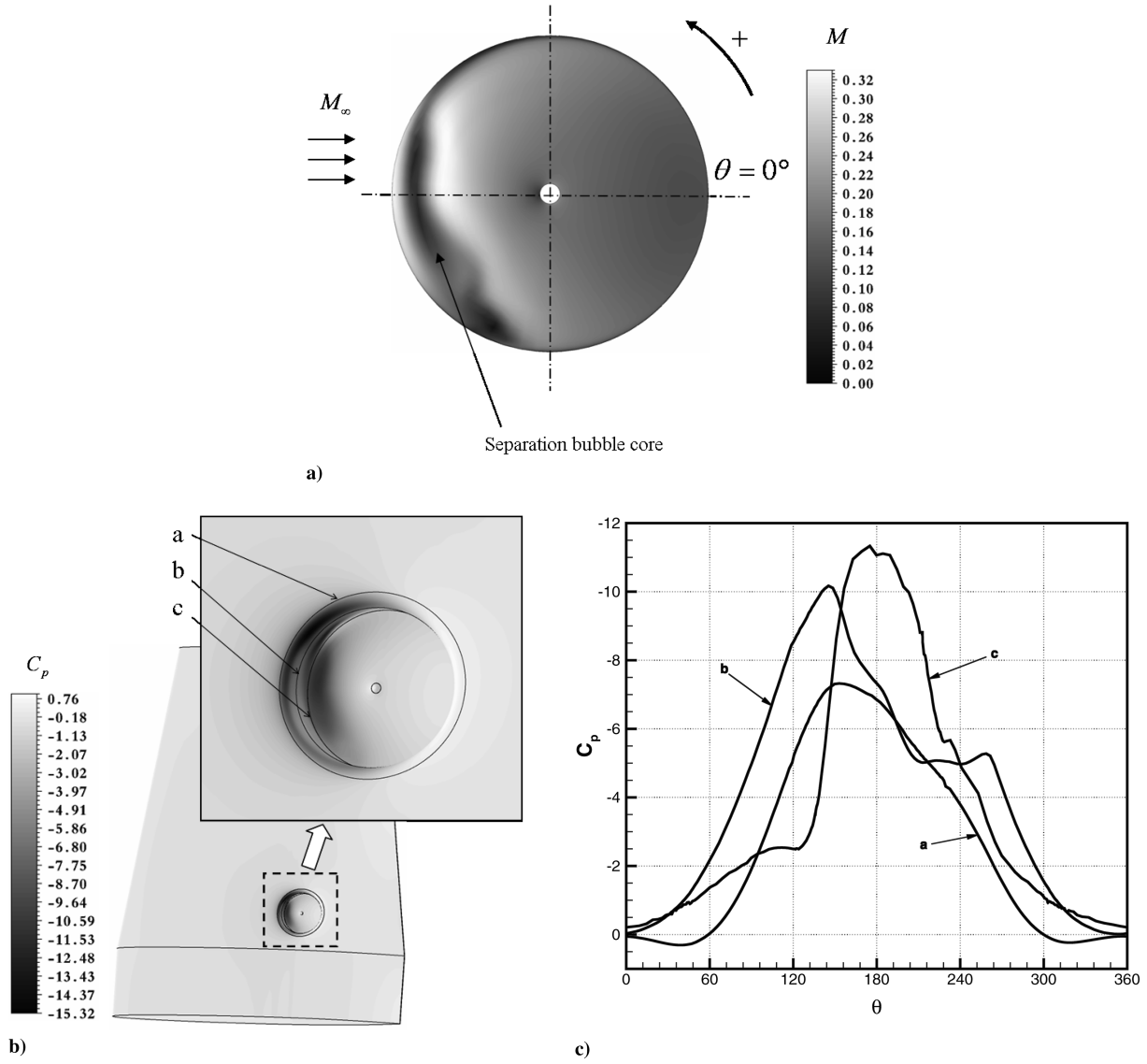

Fig. 10 Flow characteristics at sliding interface: a) Mach contours on the wing's upper sliding interface, b) pressure coefficient contours on the wing and upper sliding interface, and c) circumferential pressure distributions [$\alpha = 0$ deg, $U_\infty = 40$ m/s, and $N = 26,200$ rpm ($\mu = 0.243$)].

the inflow distortion. As noticed for $\theta = 180$ deg, an area with high velocities and low pressure is created at the fan's inflow. The back pressure generated by the crossflow clearly affects the internal pressure distribution. Thus, the fan's operating point is also affected by the back pressure and, consequently, the fan's efficiency is reduced. This conclusion is corroborated by the comparison of the thrust coefficient with the static thrust coefficient measured at zero airspeed in the wind tunnel. According to the time-averaged results C_T is 0.034, half of the static thrust coefficient. The reduced fan's performance is due to a combined effect of the inflow distortion and the back-pressure effect at the fan's exit. Inlet guide vanes, outlet guide vanes, and an inclination of the fan's rotational axis could improve the fan's performance by creating a more homogenous internal pressure distribution. The back pressure at the fan's exit would affect the fan's behavior more significantly for a fan-in-wing configuration without stator.

4. *Counter-Rotating Pair of Vortices*

As shown before, the jet is deflected by the freestream, and a backward flow is generated downstream of the fan's exit below the lower side of the wing. The jet exiting the fan's nozzle rolls up in a pair of counter-rotating vortices represented by plotted contours of eddy-viscosity distribution at several downstream positions (Fig. 13). The root section leading edge is located at $y/b = 0$ and $z/b = 0$. The maximum eddy-viscosity level is reached at $1.3c$. At this last location, the counter-rotating vortex pair exhibits a well formed kidney shape. The eddy-viscosity level decreases after reaching its maximum at $1.3c$ and remains on a significantly high level over a distance of $8c$ downstream of the nozzle. The pair of vortices clearly dominates the downstream flowfield and has an important effect on the wing's performance inducing considerable pressure drag and a loss of lift on the wing part downstream of the nozzle. This is confirmed by the chordwise pressure distribution shown in the next section (cf. Fig. 15).

IV. Comparison with the Experimental Data

In this section a comparison of the experimental data with the time-averaged URANS results is made.

A. Closed Wing Without Fan

Angle-of-attack polars obtained experimentally are presented in Fig. 14 to provide some additional insight on the wing's behavior. The ratio of the freestream velocity over the fan's rotation speed defines the tip-speed ratio μ as proposed by Hickey [22]. It characterizes the freestream capability to deflect the nozzle jet. A strong jet deflection (high μ) induces less pressure drag but also less lift, whereas a weak jet deflection (low μ) results in higher drag and higher lift coefficient [17]. The flow exiting the nozzle acts like a jet flap and, therefore, increases the circulation and the lift coefficient

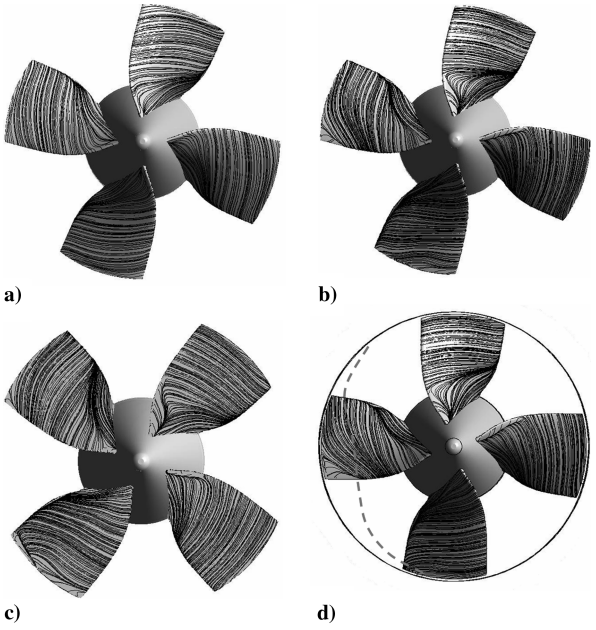

Fig. 11 Streamlines on the rotor a) based on the time-averaged velocity, and b), c), and d) based on the velocity for different mesh/rotor positions [$\alpha = 0$ deg, $U_\infty = 40$ m/s, and $N = 26,200$ rpm ($\mu = 0.243$)].

(Fig. 14a). The offset between the two lift polars is partly due to the fan's thrust and partly due to the induced lift generated by this jet-flap effect. The crossflow generated by the fan causes a significant increase of the drag coefficient compared with the reference case without a fan. The relative increase in drag tends to be higher at a high angle of attack (Fig. 14b). Considering the pitching moment, the fan inside the wing induces a nose-down pitching moment compared with the reference case (Fig. 14c).

The closed wing without a fan is simulated to give further understanding on the wing's flowfield and to serve as a reference case. Bigger differences between the numerically and experimentally obtained lift coefficient are observed at high angles of attack for the airfoil NACA 16-020. Several sections of the wing have been measured. The wind-tunnel-model airfoil shape differs slightly from the original shape. This geometrical imperfection mainly concerns the wing's rear part, which is less thick than the original airfoil. This difference affects the prediction of the trailing-edge separation. A similar trend in the model imperfection is observed for the entire model. A scanned airfoil is, therefore, substituted to the original profile in additional simulations without a fan to verify the origin of the observed discrepancies.

Furthermore, the boundary layer is imposed as laminar upstream of the suction peak. No tripping has been applied to the wind tunnel model, thus resulting in a small portion of laminar flow at the leading edge. At $\alpha = 10$ deg, 2.5% of the chord is set as laminar.

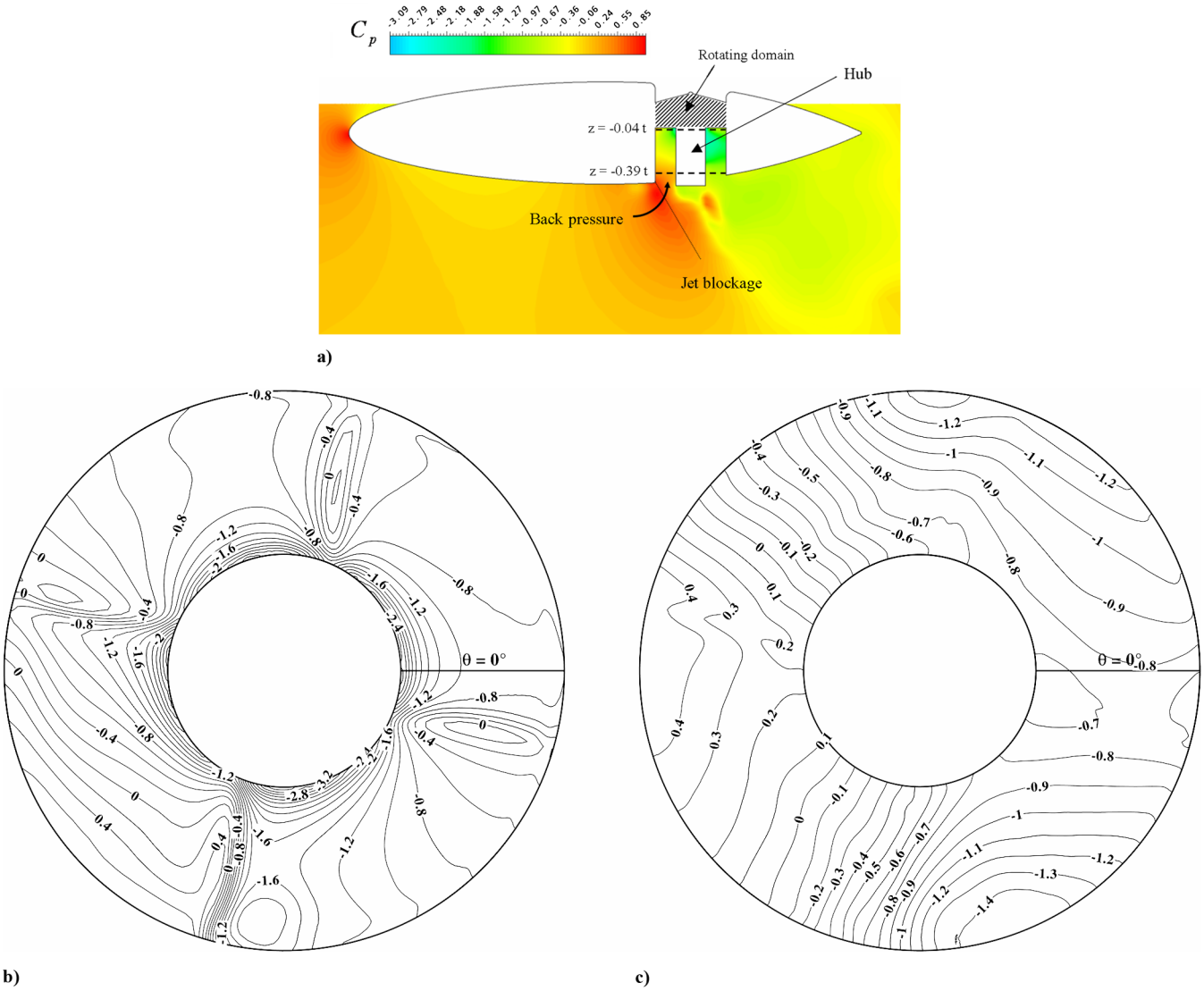

Fig. 12 C_p contours of internal sections showing a) sections' positions, b) $z = -0.04t$, and c) $z = -0.39t$ [$\alpha = 0$ deg, $U_\infty = 40$ m/s, and $N = 26,200$ rpm ($\mu = 0.243$)].

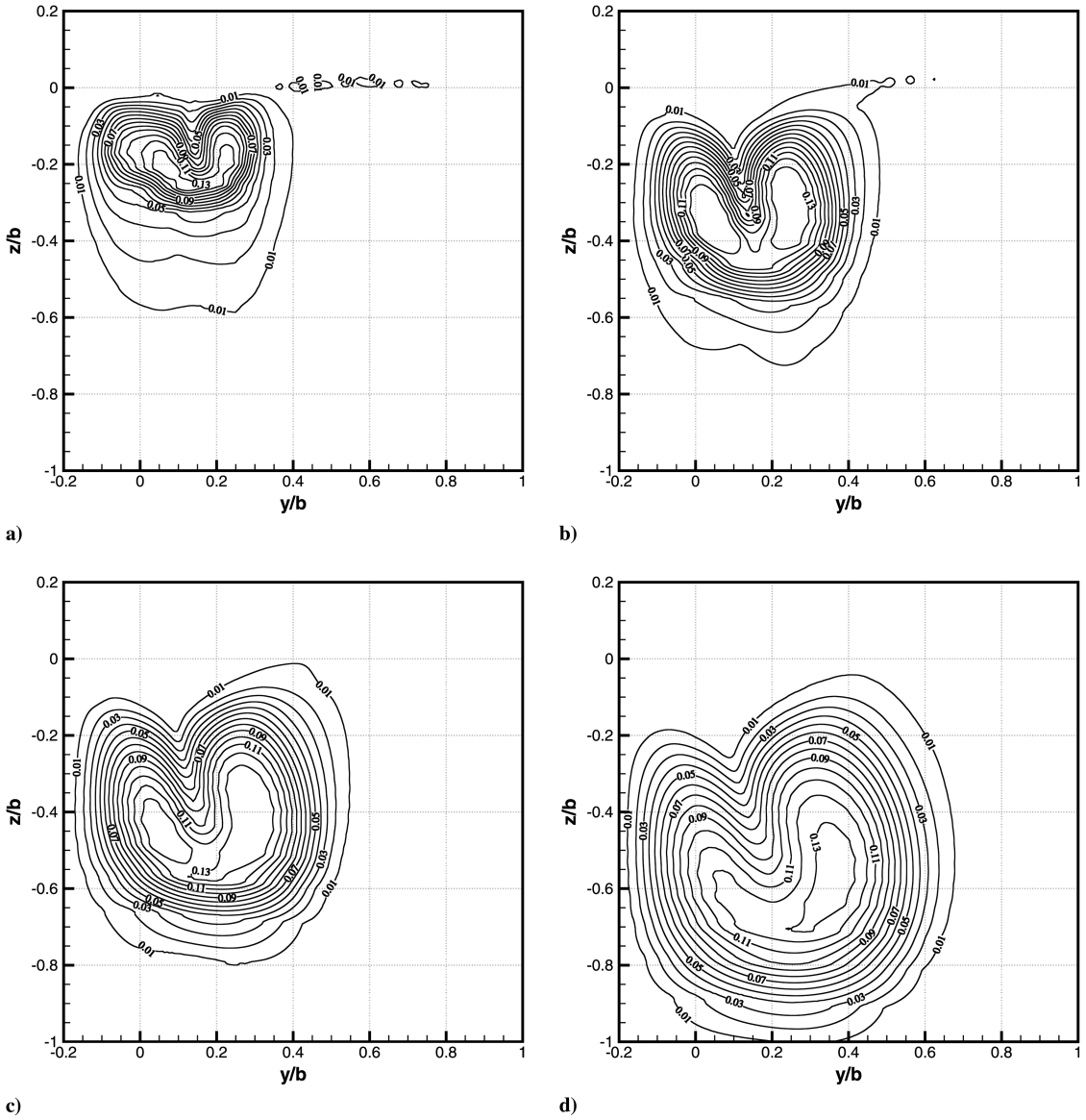

Fig. 13 Contours of eddy viscosity μ_t at several streamwise locations a) at $x/c = 1$, b) at $x/c = 1.5$, c) at $x/c = 2$, and d) at $x/c = 3$ [$\alpha = 0$ deg, $U_\infty = 40$ m/s, and $N = 26,200$ rpm ($\mu = 0.243$)].

A structured mesh is built around the geometry. As for the fan-in-wing mesh, a C-H topology is used for the domain, with the same dimensions. The grid details are as follows: 64 normal layers in the C-H mesh, 176 nodes wrapping around the airfoil, $y_+ = 0.4$ averaged over the wing, and a leading-edge spacing of $0.003c$. The total number of nodes is approximately 1×10^6. Refinements in the normal direction, at the wing tip, and around the airfoil have been conducted. No significant changes have been observed on the results. In addition, a variation of y_+ has been made. Reducing the value of y_+ improves the agreement with the experimental data. The results are presented in Table 3 and show a good agreement with the experimental data.

Table 3 Aerodynamic coefficients of the closed wing ($U_\infty = 30$ m/s)

Parameters		$\alpha = 0$ deg	$\alpha = 5$ deg	$\alpha = 10$ deg
C_L	CFD	−0.001	0.165	0.325
	Experimental	0.006	0.162	0.309
C_D	CFD	0.017	0.021	0.038
	Experimental	0.015	0.022	0.037
C_m	CFD	0.001	0.027	0.045
	Experimental	0.002	0.029	0.046

B. Fan-in-Wing Configuration

1. *Lift, Drag, and Pitching Moment*

The drag coefficients predicted by the simulation show a very good agreement with the experimental data whereas the lift coefficients exhibit differences (Table 4). The differences observed on the lift coefficient are conveyed to the pitching moment coefficient. The relative difference in the lift coefficient is less significant at $\alpha = 0$ deg than at $\alpha = 5$ deg. As mentioned before for the closed-wing simulation, the airfoil imperfection affects the lift coefficient at high angle of attack.

Table 4 Comparison of aerodynamic coefficients based on numerical simulation and experiments (case a: $\alpha = 0$ deg, $U_\infty = 40$ m/s, and $N = 26,200$ rpm; case b: $\alpha = 5$ deg, $U_\infty = 30$ m/s, and $N = 21000$ rpm)

Parameters	Case	CFD	Experimental
C_L	a	0.272	0.298
	b	0.483	0.403
C_D	a	0.097	0.101
	b	0.120	0.123
C_m	a	−0.038	−0.055
	b	−0.027	−0.007

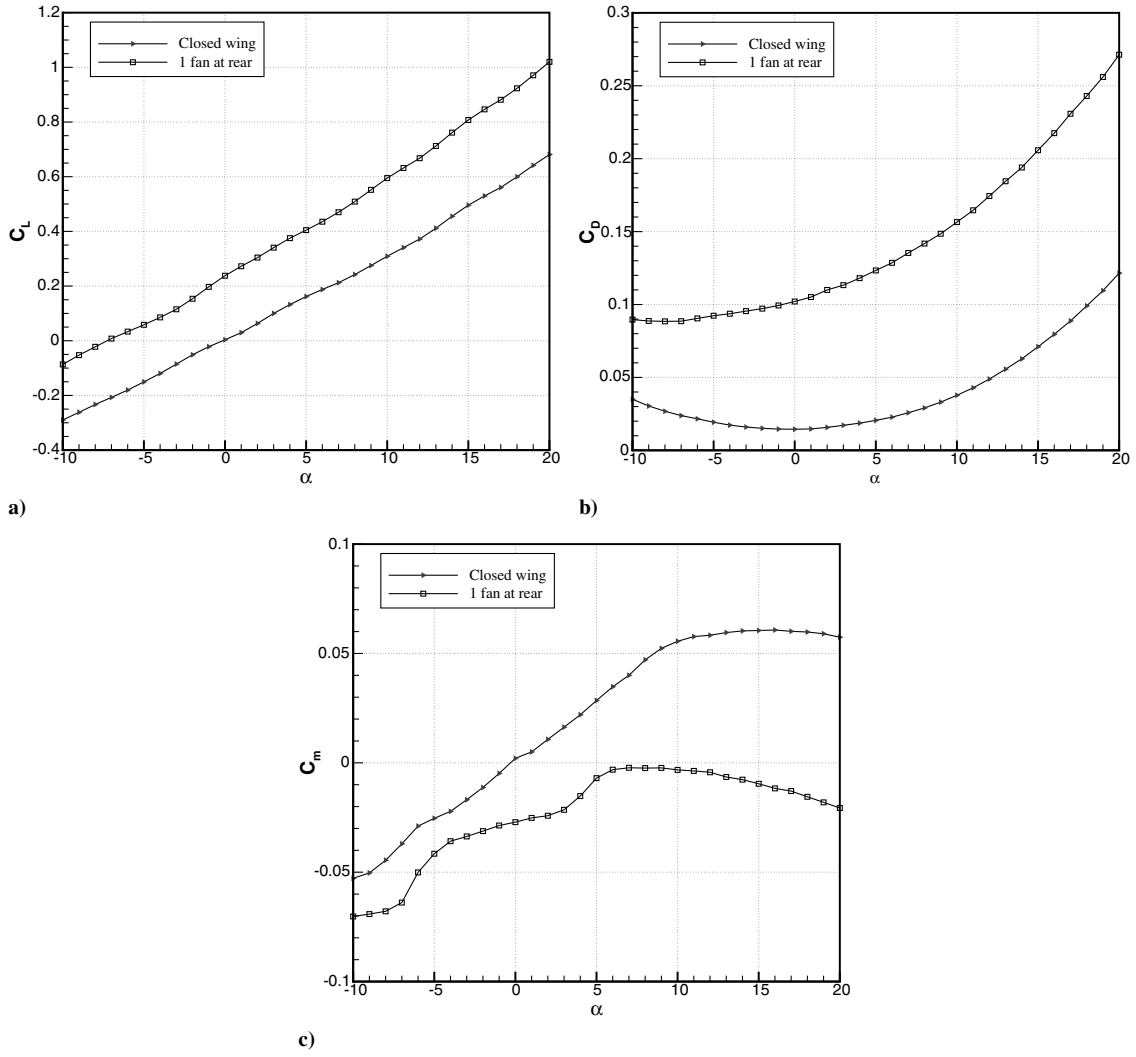

Fig. 14 Experimental aerodynamic coefficients of a) lift, b) drag, and c) pitching moment as a function of angle of attack for $U_\infty = 30$ m/s and $N = 21,000$ rpm ($\mu = 0.227$).

2. Surface Pressure Distribution

Two chordwise pressure distributions located in the spanwise direction at $\frac{1}{3}b$ and $\frac{2}{3}b$ are investigated. The suction peak on the rear part downstream of the jet, due to the jet mixing with the crossflow, shows a good agreement with the experimental measurements (Fig. 15a). The overall pressure distribution matches well with the experimental data for both chordwise distributions (Fig. 15b). Small differences are observed on the rear part of the airfoil at $\alpha = 5$ deg (Figs. 15c and 15d). Note that small pressure oscillations can be observed between 65 and 75% of the chord. It is due to an insufficient refinement in the spanwise direction far from the inlet lip, but this effect is negligible. Circumferential pressure distributions around the inlet lip show a good agreement with the experimental data (Fig. 16).

3. Surface Streamlines

Wool-tuft flow visualization provides an overview of the near-wall flow direction and indicates regions of attached and separated flow. In the simulation surface streamlines are based on the time-averaged velocity. The reattachment of the boundary layer on the wing's upper side and downstream of the fan can be seen for both numerical and experimental results (Figs. 17a and 17c). The separation at the trailing edge over this area is also relatively well described by the simulation at $\alpha = 0$ deg. However, a small separation area observed in the experimental picture, indicated by a circle in Fig. 17c, is not reproduced by the simulation. This small area occurs in a low momentum region where streamlines are ingested. It is linked to the retreating and advancing flow condition on the rotor blades identified in Sec. III. On the wing's lower side, the overall shape of the suction area appears to be well captured by the numerical simulation. The horseshoe vortex, clearly visible numerically, matches with the experimental picture (Figs. 17b and 17d). The separation occurring at the trailing edge and over the fan is also well described by the simulation at zero angle of incidence. The flow on the wing's lower side and downstream of the fan's nozzle is highly unsteady. In this area, the separation and reattachment regions vary rapidly in time. Therefore, the wool-tufts visualization cannot clearly indicate the attached and separated region.

4. Flowfield

Flowfield mapping based on stereo-PIV measurements provide quantitative velocity data for comparison downstream of the fan's exit. The PIV measurements have been performed at $1.22c$ near the trailing edge to capture the pair of counter-rotating vortices. The kidney shape as well as the location of the velocity contours is well predicted by the numerical simulation (Fig. 18). For the closed wing without a fan, the trailing-edge wake is located at the line $z \approx 0$ at $\alpha = 0$ deg. Indicated by a velocity deficit of about 0.35, for the fan-in-wing configuration (Fig. 18b), the trailing-edge wake is split up while fed into the inboard and outboard vortex, respectively. The position of the trailing-edge wake is well described by the simulation. The velocity magnitude and the position of the vortex core are also in good agreement with the experimental results (PIV results performed at $1.1c$, not presented here, corroborate these conclusions).

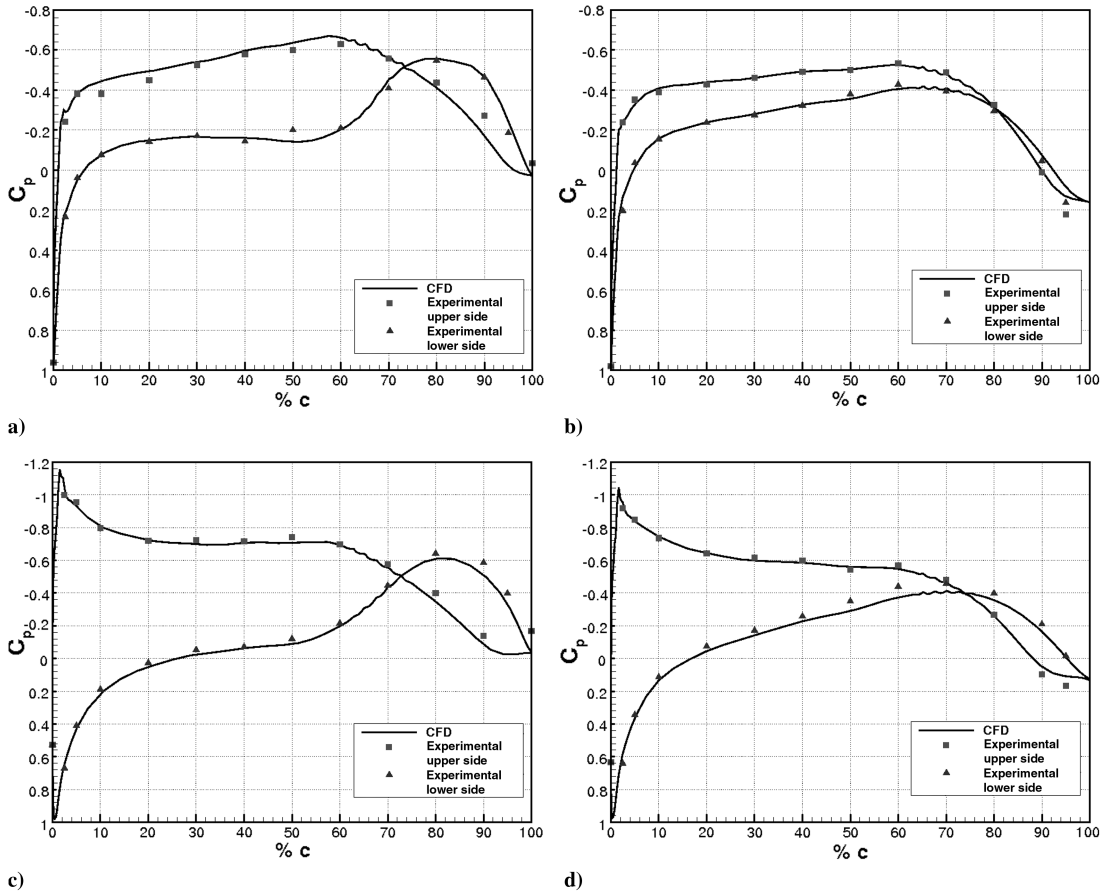

Fig. 15 Comparison of experimental and numerical chordwise pressure distribution at a) $\frac{1}{3}b$, b) $\frac{2}{3}b$ ($\alpha = 0\,\text{deg}$, $U_\infty = 40$ m/s, and $N = 26,200$ rpm), c) $\frac{1}{3}b$, d) $\frac{2}{3}b$ ($\alpha = 5\,\text{deg}$, $U_\infty = 30$ m/s, and $N = 21,000$ rpm).

V. Conclusions and Outlook

URANS simulations using the ANSYS CFX flow simulation software were conducted for a fan-in-wing configuration using a sliding mesh technique. A block-structured mesh for the entire geometry has been generated. Time-averaged results over one fan revolution were discussed for selected operating conditions and compared with experimental data. A wide range of experimental techniques, including force measurements, surface static pressure measurements, stereo PIV, and wool-tuft flow visualization, were used to proof the numerical results. The unsteady behavior of a recirculation area above the rotor blades due to the separation on the fan's inlet was analyzed. The back pressure in the internal flow due to the jet blockage upstream of the nozzle was studied. The main features encountered in a jet in crossflow are a horseshoe vortex on the wing's lower side, wake vortices, and generation and spreading of a counter-rotating vortex pair. These characteristics are predicted by the simulation for all investigated angles of attack and tip-speed ratios. A satisfying agreement was observed between the numerical results and the whole range of experimental data. The flow physics is

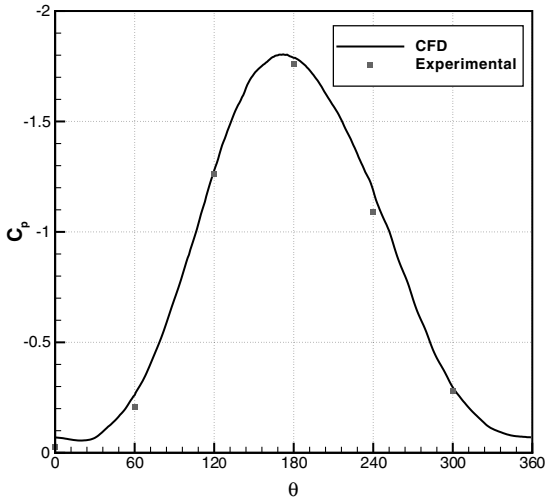

Fig. 16 Circumferential pressure distribution at $0.8D_f$ on the wing's upper side ($\alpha = 0\,\text{deg}$, $U_\infty = 40$ m/s, and $N = 26,200$ rpm).

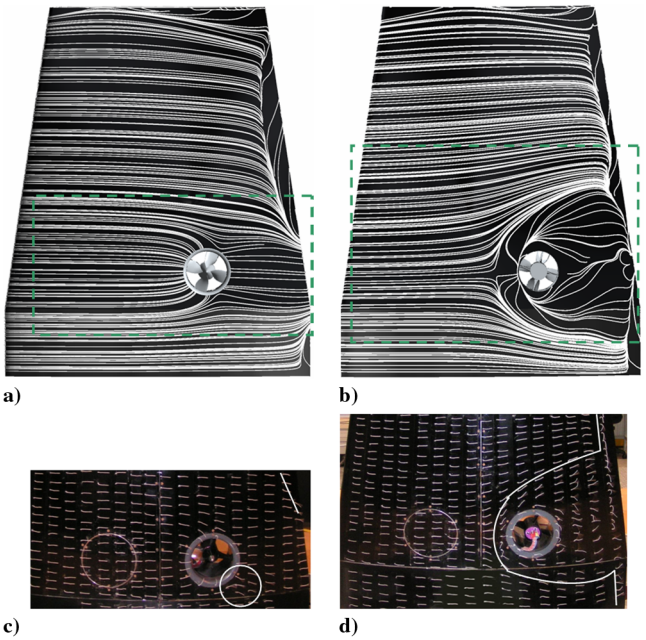

Fig. 17 Comparison of numerical surface streamlines a) on the wing's upper side and b) on the wing's lower side; and wool-tuft flow visualization c) on the wing's upper side and d) on the wing's lower side at $\alpha = 0\,\text{deg}$, $U_\infty = 40$ m/s, and $N = 26,200$ rpm ($\mu = 0.243$).

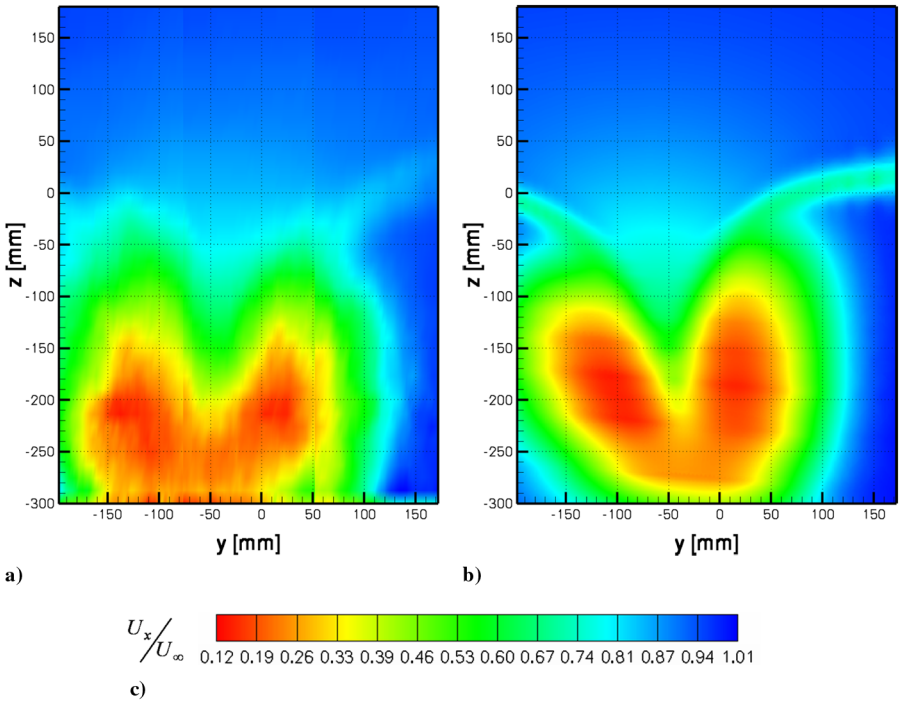

Fig. 18 Contours of streamwise velocity in a crossflow plane at $x/c = 1.22$ showing a) CFD results and b) experimental results. The PIV sheet center ($y = 0$ mm and $z = 0$ mm) is located at $x = 1.22c$, $y = 0.18b$, and $z = -0.14t$ from the wing's root chord leading edge. $\alpha = 0$ deg, $U_\infty = 40$ m/s, and $N = 26,200$ rpm ($\mu = 0.243$).

well reproduced by the simulation. Further analysis will be carried out on the flow topology, the influence of the turbulence model, and the major parameters of a fan-in-wing configuration.

Acknowledgments

The support of these investigations by the Bauhaus Luftfahrt e. V. and especially the comments of Corin Gologan and Jost Seifert are gratefully acknowledged. The authors would like to thank ANSYS CFX for providing the flow simulation software and Daniel Schübeler for providing the fan CAD data.

References

[1] Diedrich, J. H., "Summary of Model VTOL Lift Fan Tests Conducted at NASA Lewis Research Center," NASA TM X-71778, July 1975.

[2] Hickey, D. H., and Kirk, J. V., "Survey of Lift-Fan Aerodynamic Technology," NASA CR-177615, Sept. 1993.

[3] Przedpelski, Z. J., "Lift Fan Technology Studies," NASA CR-761, April 1967.

[4] Schaub, U. W., "Experimental Investigation of Flow Distortion in Fan-in-Wing Inlets," *Journal of Aircraft*, Vol. 5, No. 5, 1968, pp. 473–478. doi:10.2514/3.43969

[5] Lieblein, S., Yuska, J. A., and Diedrich, J. H., "Performance Characteristics of a Model VTOL Lift Fan in Crossflow," *Journal of Aircraft*, Vol. 10, No. 3, 1973, pp. 131–136. doi:10.2514/3.44357

[6] Saddington, A. J., and Knowles, K. A., "A Review of Out-of-Ground-Effect Propulsion-Induced Interference on STOVL Aircraft," *Progress in Aerospace Sciences*, Vol. 41, Nos. 3–4, 2005, pp. 175–191. doi:10.1016/j.paerosci.2005.03.002

[7] Kuhn, R. E., Margason, R. J., and Curtis, P., "Transition Out-of-Ground Effect," *Jet Induced Effects: The Aerodynamics of Jet and Fan Powered V/STOL Aircraft in Hover and Transition*, edited by F. K. Lu, Vol. 217, Progress in Astronautics and Aeronautics, AIAA, New York, 2007, pp. 53–92.

[8] Kelso, R. M., Lim, T. T., and Perry, A. E., "An Experimental Study of Round Jets in Crossflow," *Journal of Fluid Mechanics*, Vol. 306, 1996, pp. 111–114. doi:10.1017/S0022112096001255

[9] Kelso, R. M., and Smits, A. J., "Horseshoe Vortex Systems Resulting from the Interaction Between the Laminar Boundary Layer and a Transverse Jet," *Physics of Fluids*, Vol. 7, No. 1, 1995, pp. 153–158. doi:10.1063/1.868736

[10] Fric, T. F., and Roshko, A., "Vortical Structure in the Wake of a Transverse Jet," *Journal of Fluid Mechanics*, Vol. 279, 1994, pp. 1–47. doi:10.1017/S0022112094003800

[11] Baker, C. J., "The Laminar Horseshoe Vortex," *Journal of Fluid Mechanics*, Vol. 95, 1979, pp. 347–367. doi:10.1017/S0022112079001506

[12] Cortelezzi, L., and Karagozian, A. R., "On the Formation of the Counter-Rotating Vortex Pair in Transverse Jets," *Journal of Fluid Mechanics*, Vol. 446, 2001, pp. 347–373.doi:.1017/S0022112001005894

[13] Smith, S. H., and Mungal, M. G., "Mixing, Structure and Scaling of the Jet in Crossflow," *Journal of Fluid Mechanics*, Vol. 357, 1998, pp. 83–122. doi:10.1017/S0022112097007891

[14] Kamotani, Y., and Greber, I., "Experiments on a Turbulent Jet in Crossflow," *AIAA Journal*, Vol. 10, No. 11, 1972, pp. 1425–1429. doi:10.2514/3.50386

[15] Kummer, J. D., and Dang, T. Q., "High-Lift Propulsive Airfoil Integrated Crossflow Fan," *Journal of Aircraft*, Vol. 43, No. 4, 2006, pp. 1059–1068. doi:10.2514/1.17610

[16] Dygert, R. K., and Dang, T. Q., "Experimental Investigation of Embedded Crossflow Fan for Airfoil Propulsion/Circulation Control," *Proceedings of the 45th Aerospace Sciences Meeting and Exhibit*, AIAA Paper 2007-368, Jan. 2007.

[17] Thouault, N., Gologan, C., Breitsamter, C., Adams, N. A., and Seifert, J., "Experimental Investigations on Generic Fan-In-Wing Configurations," *Proceedings of the International Powered Lift Conference*, AIAA Paper pa8, July 2008.

[18] Kummer, J. D., "Crossflow Fan Propulsive Airfoil Concept," *Simulation of the Crossflow Fan and Application to a Propulsive Airfoil Concept*, Ph.D. Dissertation, Syracuse Univ., Syracuse, NY, Aug. 2006, pp. 176–212.

[19] Melber-Wilbending, S., Brodersen, O., Kallinderis, Y., Wilhelm, R., Sutcliffe, M., Wild, J., and Ronzheimer, A., "Part I Grid Generation," *MEGAFLOW—Numerical Flow Simulation for Aircraft Design*, Vol. 89, Springer–Verlag, Berlin, 2005, pp. 3–27.

[20] Menter, F. R., "Two-Equation Eddy-Viscosity Turbulence Models for Engineering Applications," *AIAA Journal*, Vol. 32, No. 8, 1994, pp. 1598–1605. doi:10.2514/3.12149

[21] "ANSYS CFX-Solver Theory Guide, Release 11.0," Dec. 2006, pp. 119–121.

[22] Hickey, D. H., and Ellis, D. R., "Wind-Tunnel Tests of a Semispan Wing with a Fan Rotating in the Plane of the Wing," NASA TN D-88, Oct. 1959.